Wall-jet evolution during plume-surface interaction using PLIF imaging

Neil S. Rodrigues[1]
NASA Langley Research Center, Hampton, VA, 23681, USA

Ross A. Burns[2]
ViGYAN, Inc., Hampton, VA, 23666, USA

Olivia K. Tyrrell[3] and Paul M. Danehy[4]
NASA Langley Research Center, Hampton, VA, 23681 USA

Planar laser-induced fluorescence (PLIF) flow visualization was used to examine the spatial evolution for the wall-jet formed by an impinging supersonic jet in a large-scale vacuum environment. This canonical configuration is representative of the plume-surface interaction (PSI) induced by a rocket exhaust plume impinging on the planetary surface at lunar-relevant and Martian-relevant environments. PLIF flow visualization of the very low-density environment (as low as ~0.006% of standard atmospheric density) was performed using seeded nitric oxide in a nitrogen flow at three test conditions. Two conditions are representative of the lunar environment, and one is representative of the Martian environment. The combined images from two simultaneous PLIF views were used to construct a 2D slice of the flowfield spanning approximately 150 mm in height (determined by the laser sheet) and 500 mm in width (determined by the camera views). The three test conditions showed different behavior for the wall-jet, largely due to the different levels of lifting above the surface and the appearance of a physical process similar to a Kelvin–Helmholtz instability for the Martian-relevant case, which appeared to create a dramatic expansion of the wall-jet height with increased radial distance.

I. Introduction

During powered descent and landing of spacecraft on planetary bodies, such as the Moon and Mars, significant risks to the vehicle, landing site, and nearby infrastructure exist due to interactions between rocket exhaust plumes and the unimproved (i.e., no landing pad) planetary surface. Ground test data using scaled and canonical configurations provide critical insights of the underlying plume-surface interaction (PSI) phenomena by investigating sensitivities of relevant gas and granular physics parameters, as well as global parameters such as the spacecraft thrust, altitude, and ambient environment. Three ground test campaigns were recently completed at the NASA Marshall Space Flight Center to support this endeavor. The first ground test was performed in a 15-ft diameter vacuum chamber and used several different regolith simulants for the purposes of characterizing erosion behavior and ejecta phenomena at both lunar-relevant and Martian-relevant ambient pressure conditions [1-4]. Erosion behavior from this ground test was used to propose scaling laws for plume-induced granular cratering [5]. The second ground test was also performed in the 15-ft chamber, with an instrumented flat plate replacing the regolith soil bin. The third ground test, which is the focus of the current work, was performed in an adjacent 20-ft vacuum chamber and investigated the induced flowfield of the same supersonic jet impinging upon a flat plate. Flow visualization was performed using planar laser-

[1] Optical Physicist, Advanced Measurements and Data Systems Branch, AIAA Member.
[2] Senior Research Engineer, Advanced Measurements and Data Systems Branch.
[3] Research Engineer, Advanced Measurements and Data Systems Branch, AIAA Member.
[4] Senior Technologist, Advanced Measurements and Data Systems Branch, AIAA Associate Fellow

induced fluorescence (PLIF), which is a molecular-based, planar, 2D (two-dimensional) measurement technique that can be used to visualize flowfields of a targeted atoms or molecules [6].

Results from different aspects of the 20-ft vacuum chamber test have been reported in several publications. The paper by Rodrigues *et al.* [7] provides a broad overview on the entire test campaign at the 20-ft vacuum chamber facility. A comprehensive description of the complex experimental systems used for this test and detailed data analysis for select test cases spanning lunar-relevant and Martian-relevant conditions were the focus of a subsequent Rodrigues *et al.* paper [8]. The paper by Tyrrell *et al*. [9] considers the impact of PSI ground-test design decisions on the plume impingement flowfield, namely a half-space vs. a full-space design. The plume impingement behavior and its relationship to impingement pressure at Martian-relevant conditions spanning eight different nozzle flow and height test combinations was the focus of a different Rodrigues *et al.* paper [10]. A concurrent paper by Rubio *et al.* [11] investigates a potential flow instability based on the evidence of ejecta streaks in the 15-ft test campaign and uses PLIF data from the 20-ft chamber to formulate a hypothesis.

The PLIF data from the 20-ft vacuum chamber test described in the literature thus far is based on a single, near-field PLIF camera view that focuses on the plume impingement region. In fact, the limited flow visualization in the PSI literature has exclusively focused on the primary plume expansion and the stagnation shock behavior [12]. While important, this does not consider the high velocity wall-jet emitting from the location of impingement that also contributes to erosion and transport of eroded ejecta. In this paper, we present and discuss fluorescence images from a secondary PLIF camera showing the spatial evolution of the so-called wall-jet that is formed near the impingement region and propagates away from the nozzle centerline. A two camera PLIF measurement system was essential to maintain the spatial resolution required to image flow structures in the near-field while simultaneous imaging the wall-jet at a reduced resolution. The secondary PLIF camera was only available for select test runs, and results from three distinct test runs are presented in this paper. Instantaneous (< 200 ns exposure) and average PLIF images from similar

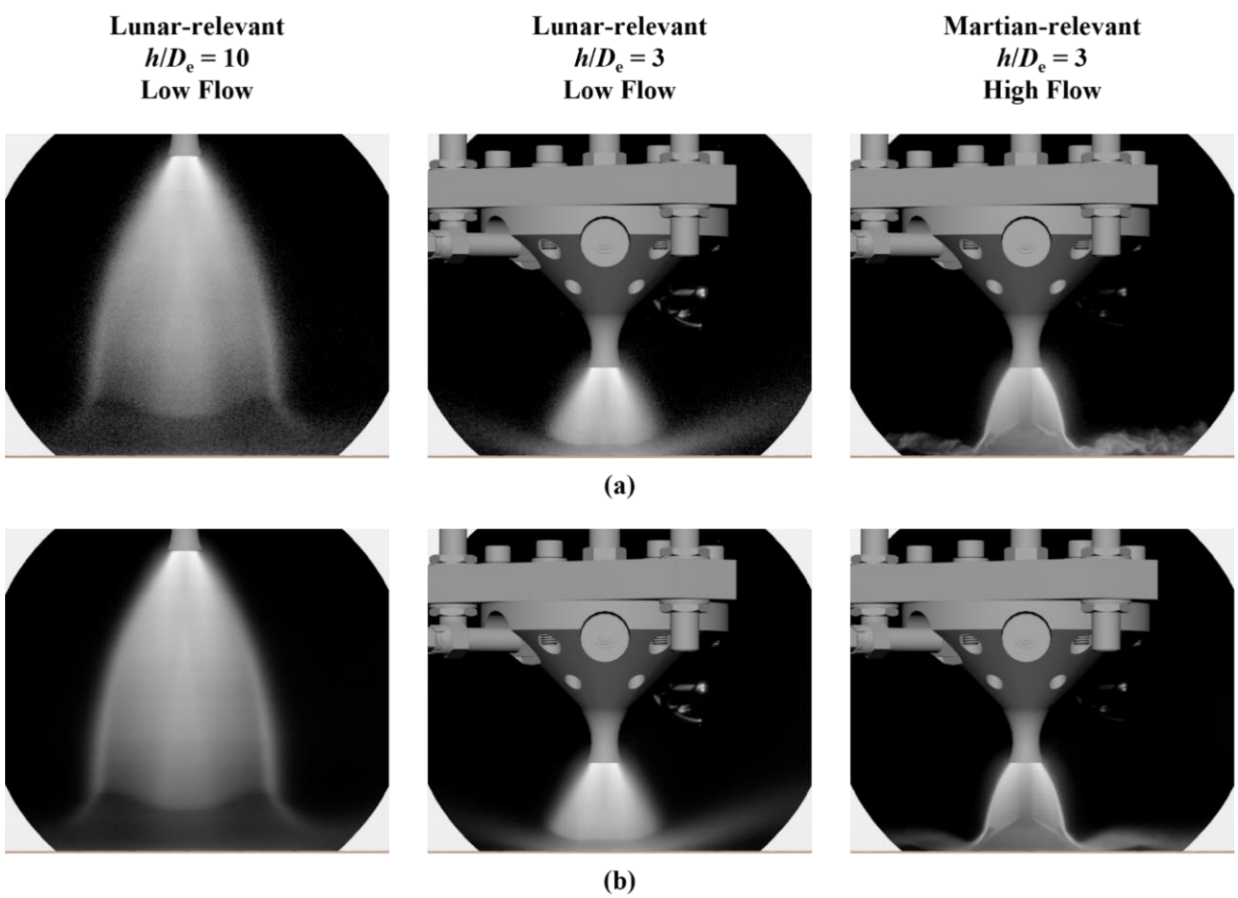

Fig. 1. (a) Instantaneous and (b) averaged PLIF images from the plume impingement camera, shown in logarithmic scale, at three test conditions similar to the conditions presented in this paper.

test conditions where only the plume impingement camera was installed have been presented previously in Refs. 7-10 and are shown in Fig. 1 for context. The evolution of the wall-jet, which is experimentally described by this paper for the first time in the literature, was captured using a second PLIF camera that featured a wider field of view through the utilization of a shallow angle relative to the laser sheet.

II. Experimental Systems

The experimental systems for the plume-surface interaction test performed in the 20-ft diameter vacuum chamber at the NASA Marshall Space Flight Center have been reported in detail in previous publications [7-8] and only a brief description is provided here. Key sub-systems for the experiment include: the plume impingement apparatus, the vacuum chamber facility, and the planar laser-induced fluorescence systems. A CAD schematic of the vacuum chamber with the test article and PLIF diagnostics is shown in Fig. 2.

The test article primarily consisted of a supersonic nozzle assembly and an impingement plate assembly; both assemblies are discussed in detail in Refs. 7-8. The nozzle assembly was installed on a vertical translation stage, which allowed the height of the nozzle exit relative to the surface of the impingement plate to be remotely varied. The supersonic nozzle, which featured an area ratio $A/A^* = 31.7$ and an exit diameter $D_e = 1.38$ cm, was oriented perpendicular to the impingement plate. Heated nitrogen premixed with nitric oxide was used as the test gas. The exit Mach number based on the area ratio and the specific heat ratio of the test gas was approximately 5.3. The stagnation pressure and stagnation temperature of the nozzle were recorded by the 100 Hz facility DAQ for each test

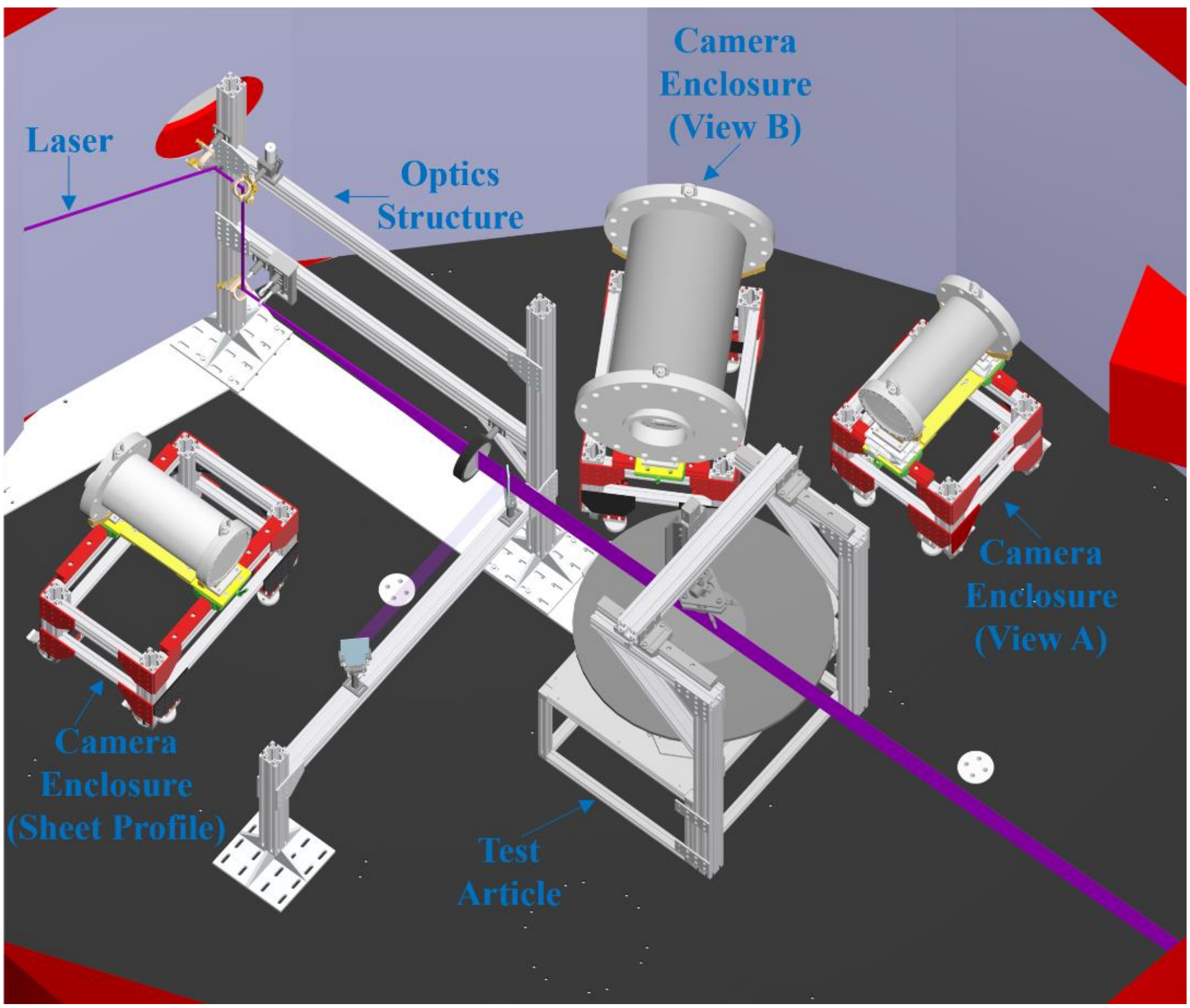

Fig. 2. CAD schematic of the vacuum chamber with the test article and PLIF instrument, including two camera enclosures for simultaneous *plume impingement* (view A) and *wall-jet evolution* (view B) imaging.

Table 1. Test conditions for results presented in this paper.

		[-]	[Pa]	[kPa]
		h/D_e	P_a	P_0
Lunar-relevant	Case I	10	3.8	38.7
	Case II	3	1.8	38.3
Martian-relevant	Case III	3	584 → 618	743 → 962

run. The diameter of the impingement plate assembly, which consisted of an instrumented inner plate and an annular outer plate, was approximately 86 cm or sixty-six times that of the nozzle exit diameter. The impingement plate featured both low-frequency and high-frequency pressure instrumentation as described in Ref. 7. However, the impingement pressure measurements are outside the scope of the present work, which focuses on the fluorescence imaging.

The three distinct test conditions reported in this abstract, which are similar to the three test conditions shown in Fig. 1, are tabulated in Table 1. The lunar-relevant conditions with an ambient pressure $P_a \sim O(1\text{ Pa})$ correspond to Case I and Case II. Case I represents a higher dimensionless altitude corresponding to $h/D_e = 10$, whereas Case II represents a lower dimensionless altitude corresponding to $h/D_e = 3$. A steady-state jet stagnation pressure of approximately $P_0 = 38$ kPa was used for both lunar-relevant conditions. Case III features a Martian-relevant ambient pressure $P_a \sim O(600\text{ Pa})$ and $h/D_e = 3$. The Case III data presented in this abstract also features a higher jet stagnation pressure and the jet start-up transient process is also illustrated.

The PLIF laser systems were located in a room adjacent to the vacuum chamber and primarily consisted of a tunable ultraviolet (UV) laser beam with a wavelength near 226 nm, pulse duration of 10 ns, and repetition-rate of 10 Hz. In addition to Refs. 7-8, additional details of the PLIF laser system can be found in Ref. 13. The PLIF laser beam was brought into the vacuum chamber through a UV-transmissive viewport and was directed to the test article using dielectric mirrors that were installed on remote-controlled mirror mounts. A lens system consisting of a cylindrical and spherical lens was used to form the laser beam into a 2D laser sheet, which was aligned to pass through the centerline of the jet. A glass plate was used to direct ~1% of the laser sheet energy towards a diffuser plate, which was used with an additional visible CCD camera for laser monitoring purposes. The visible CCD camera, which monitored the laser sheet using blue fluorescence from the glass diffuser plate, was located within a separate camera enclosure and featured a 25-mm focal length *f*/1.4 visible camera lens.

Fluorescence resulting from the laser-induced electronic excitation of nitric oxide (NO) using the Q-branch bandhead near 226 nm was captured by two different intensified sCMOS cameras that were located within pressurized enclosures near the test article. The plume impingement camera, denoted as *view A*, was equipped with a 100-mm focal length *f*/2.8 UV camera lens. The field of view was centered near the nozzle in the horizontal direction and allowed the entire vertical plume to be visualized for the range of nozzle heights tested. Fluorescence images from view A have previously been discussed in Refs. 7-10. The wall-jet evolution camera, denoted as *view B*, was equipped with a 45-mm focal length *f*/1.8 UV camera lens in a Scheimpflug configuration. Both cameras were externally triggered to allow images to be acquired simultaneously. The camera was angled such that the field-of-view covered from the edge of the primary plume exiting the nozzle to one edge of the impingement plate. Data from this camera, which has not been reported in any previous publications, allowed the entire wall-jet to be imaged from its formation near the nozzle centerline to the edge of the impingement plate. The spatial overlap between the two views at the edge of the primary plume structure (measured from the right edge of view A to the left edge of view B) was approximately 23 mm.

Custom codes were developed in MATLAB® to process the PLIF images, with nearly identical processes followed for the two cameras. The PLIF images were first subtracted with an average background image obtained with the laser firing and the jet off (an average of 10 images acquired over 1 second). A flat-field correction was performed for the view A images prior to this subtraction to remove the fixed-pattern intensifier structure. A flat field calibration was not available for the view B images and this correction was thus not performed for the present work. The view A images were spatially calibrated using an in-house dewarping code based on the pinhole model computed using Tsai's method [14]. The view B images were acquired at a significant angle of approximately 60 degrees with respect to the laser sheet propagation, instead of the nearly orthogonal (with respect to the laser sheet propagation) angle for view A. Average PLIF images from view B, computed using a sequence of 40 instantaneous images, at the three test conditions described in this work are shown in Fig. 3(a). All three images show the edge of the primary plume on the left side, with the wall-jet propagating from left-to-right. A different, custom dewarping code was adapted for this work to accommodate two different dotcard calibration targets spanning the wide field of view. This dewarping algorithm utilized polynomial dewarping; bivariate, 3rd-order polynomials were fit to each segment of the calibration

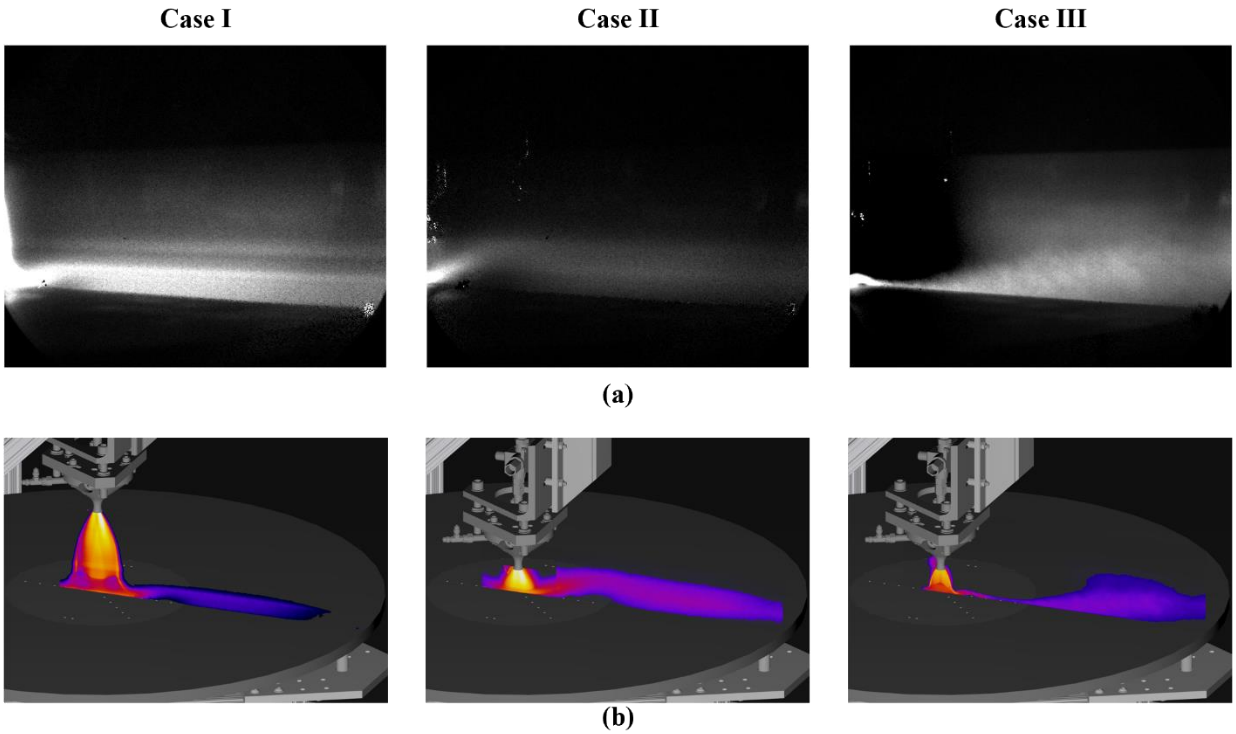

Fig. 3. (a) Average PLIF images from the secondary camera (view B), shown in linear scale, after performing a subtraction with the pre-jet background image and before performing the image dewarping and subsequent image processing operations for the three Cases. (b) Composite average image from two camera views (view A and view B) for Case I to provide context of the data in terms of the experimental set-up. The maximum value of the grayscale and color scales are arbitrary and generally adjusted to highlight the wall-jet.

target. The view B data was separated into two sections corresponding to each of these polynomials and accordingly dewarped. After dewarping both sections of the view B image, the segments were stitched together at the location that corresponded to the minimum cumulative error of the two polynomial fits. The images were then mapped onto a uniform grid using Delaunay triangulation to complete the dewarping process. After image dewarping, a 2×2 pixel binning was applied for both views. The images were cropped to the primary regions of jet flow and aligned such that the origin of the radial axis r was at the nozzle centerline and the origin of the vertical axis z was at the impingement plate. A 2D median filter was applied to both images, however the window of the median filter for the view A was approximately 1 mm × 1 mm, while a larger window of approximately 5 mm × 5 mm was used with view B to improve the signal-to-noise of the images. The larger filter window compensated for the reduced fluorescence signal of the wall-jet, which features particularly low gas densities for the lunar-relevant cases due to the near-vacuum environment. The PLIF images were combined using aspects of the aspects of the Virtual Diagnostics Interface (ViDI) described by Schwartz and Fleming [15] and are shown in Fig. 3(b) to provide context on the camera view in Fig. 3(a). The PLIF images were also incorporated into Tecplot®, where they were combined with a schematic of the supersonic nozzle for the purpose of showing spatial locations of key features for the plume impingement and wall-jet behavior. These images are shown in the following section.

III. Results and Discussion

A. Lunar-relevant

The lunar-relevant images in Fig. 1 imply that the plume impingement flow is highly laminar at the test conditions corresponding to Case I and Case II, as a lack of notable difference exists between the mean and instantaneous images. Despite the relatively high gas density regions captured with the primary camera, the instantaneous image in Fig. 1(a) appears somewhat grainy, due to the low fluorescence signals at these very low density conditions. With increasing radial distances away from both the stagnation shock and the tail shock, the pressure throughout the wall-jet is expected to be similar to the ambient pressure. The temperature is expected to be similar to the stagnation temperature of the nozzle. Therefore, very low fluorescence signals are expected in the wall-jet due to the approximate gas density of $7 \cdot 10^{-5}$ kg/m^3, based on $T \sim O(500\text{ K})$ and $P \sim O(10\text{ Pa})$, which corresponds to approximately 0.006% of standard atmospheric density conditions. Indeed, relatively low fluorescence signal levels were observed in the instantaneous images with the view B camera at the lunar-relevant conditions. Given the low signal levels and the laminar nature of the flow at these conditions, only average images (based on a sequence of 40 instantaneous images or 4 seconds of data) of the wall-jet are presented.

A combined average PLIF image from both camera views is shown in Fig. 4 for the Case I flow: $h/D_e = 10$, $P_a = 3.8$ Pa, and $P_0 = 38.7$ kPa. The images are shown in logarithmic scale with a sketch of the supersonic nozzle for context. The left side of the image highlights the plume impingement behavior including features such as the jet core and reflection point, the barrel-like plume shape, and the stagnation shock. Notably, the stagnation shock appears to be parallel to the plate within the jet core and curves significantly upward in the region between the jet core and the jet edge. The tail shock and the initial formation of the wall-jet can also be clearly seen. Here it is apparent that the wall-jet lifts off the impinging plate near $r = 80$ mm and returns to the impingement plate near $r = 150$ mm.

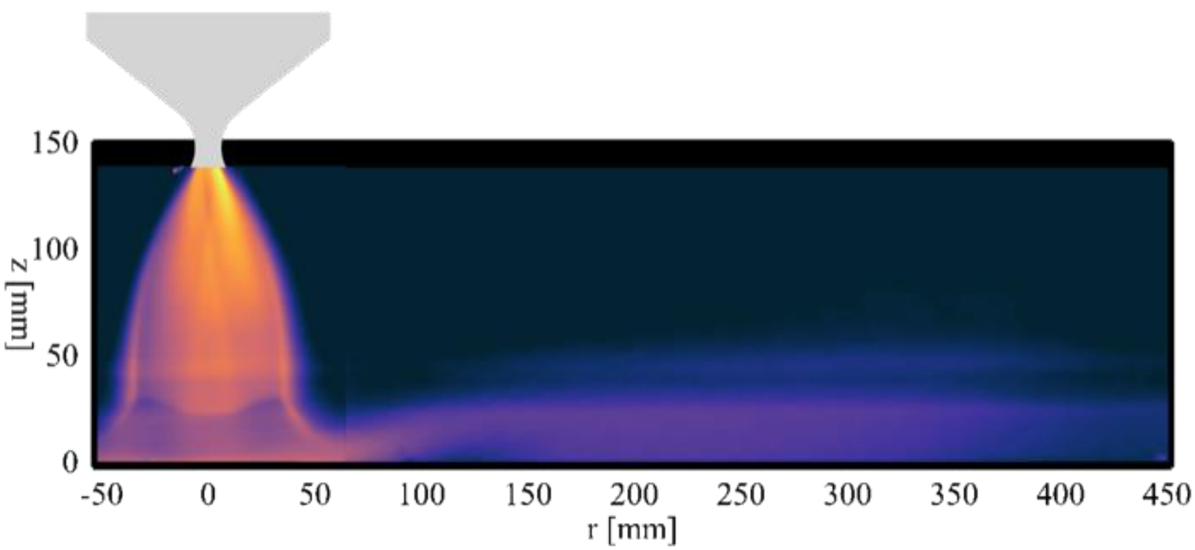

Fig. 4. Combined average PLIF image from the two camera views, shown in a logarithmic intensity scale, illustrating the plume impingement and wall-jet evolution at $P_a = 3.8$ Pa, $P_0 = 39$ kPa, and $h/D_e = 10$ (Case I).

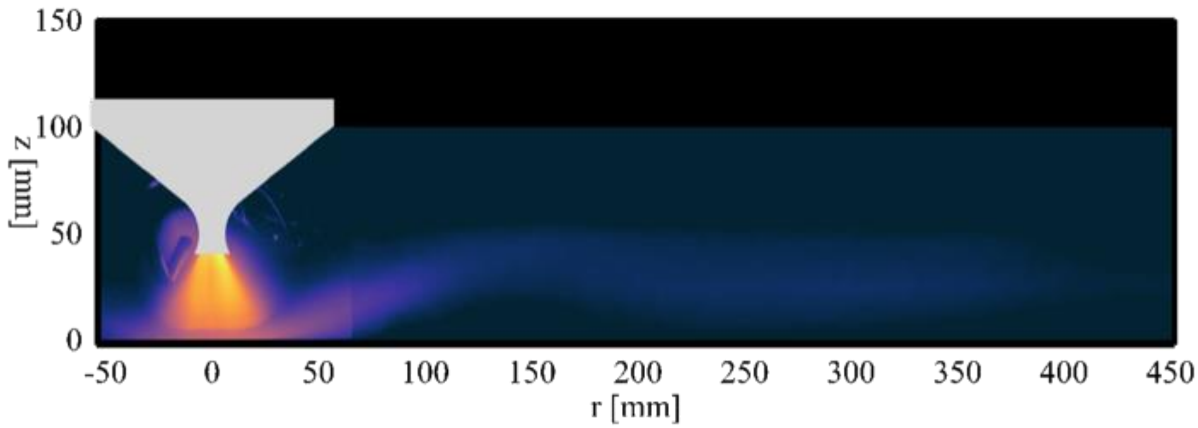

Fig. 5. Combined average PLIF image from the two camera views, shown in a logarithmic intensity scale, illustrating the plume impingement and wall-jet evolution at $P_a = 1.8$ Pa, $P_0 = 38$ kPa, and $h/D_e = 3$ (Case II).

Furthermore, the maximum height of the wall-jet appears to be near z = 50 mm. However, in the current image, background fluorescence from the build-up of the NO-N_2 mixture in the vacuum chamber during the run results in some fluorescence in the background, which makes it difficult for edge tracking algorithms to differentiate between the fluorescence from the wall-jet and the ambient gas. This background interference effect, in terms of clearly measuring the wall-jet height, is exasperated by nonuniformities in the laser sheet (i.e., a spatial distribution for laser intensity) that is inducing the fluorescence.

A composite average PLIF image at the Case II condition (P_a = 1.8 Pa, and P_0 = 38.3 kPa) featuring similar jet and ambient pressures to Case I but at h/D_e = 3 is shown in Fig. 5. Some artifacts of the experimental systems, such as cables for the nozzle heaters and instrumentation, are also visible in the PLIF image near the nozzle exit for this particular test run. The plume-impingement behavior on the left side (near r = 0 mm) shows a very different impingement behavior compared to the Case I condition in Fig. 4. A stagnation shock that is closer to the surface and nearly parallel to it can be observed. A lifted wall-jet at a greater angle with respect to the surface can also be seen. The right side of the image more clearly shows the wall-jet evolution, including the lifted behavior near r = 60 mm and return towards the surface near r = 200 mm. The height of the wall-jet is more clearly distinguishable in Fig. 5 and appears to reach a maximum height near z = 50 mm.

B. Martian-relevant

The average PLIF image at the Case III Martian-relevant condition is shown in Fig. 6. The plume impingement behavior is very different for this case compared to Case II, due to the combination of the greater jet stagnation pressure and the elevated ambient pressure. The differences in the primary impingement behavior for this jet flow are further described in Ref. 8. Furthermore, the color scale in Fig. 6 is arranged such that the higher density jet region of the primary plume upstream of the stagnation shock is saturated in order to focus on the evolution of the wall-jet. Although the average image has smeared the unsteady structures in the flow, it is still valuable to map the shape of the wall-jet as it spatially evolves from the stagnation shock. While the lifted aspect of the wall jet can be seen clearly near r = 50 mm, the wall-jet appears to return to the surface near r = 70 mm and continues to radially propagate near the surface. Instabilities inherent to the wall-jet propagation, hypothesized to be similar to a Kelvin–Helmholtz instability, result in a rapid expansion of the wall-jet starting from approximately r = 150 mm. The densities in the wall-jet are expected to be $O(10^{-3}\ \mathrm{kg/m^3})$ and therefore the instantaneous images have sufficient signal above the noise floor and background interferences to indicate the jet structure.

Combined simultaneous, instantaneous PLIF images during the jet start-up transient for Case III are shown in Fig. 7. These images offer snapshots of the jet start-up phase as the stagnation pressure increases in a nonlinear and non-monotonic manner as discussed in Ref. 8. The initial ambient pressure was slightly lower at P_a = 584 Pa and the reported ambient pressure of P_a = 618 Pa in Fig. 6 is due to the chamber pressure increasing during the test run. The instantaneous snapshots correspond to: P_0 = 743 kPa in Fig. 7(a), P_0 = 830 kPa in Fig. 7(b), and P_0 = 794 kPa in Fig. 7(c). The instantaneous images show that the wall-jet evolution is a highly unsteady process based on rather corrugated flow structure. The spatial evolution of the wall-jet and in particular the large-scale flow structures at

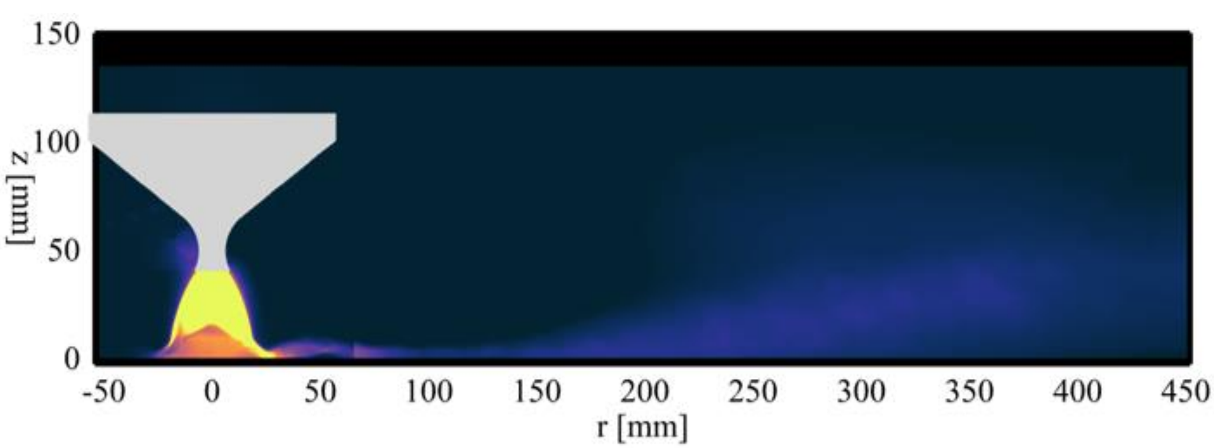

Fig. 6. Combined average PLIF image from the two camera views, shown in a linear intensity scale, illustrating the plume impingement and wall-jet evolution at P_a = 618 Pa, P_0 = 38 kPa, and h/D_e = 3 (Case III).

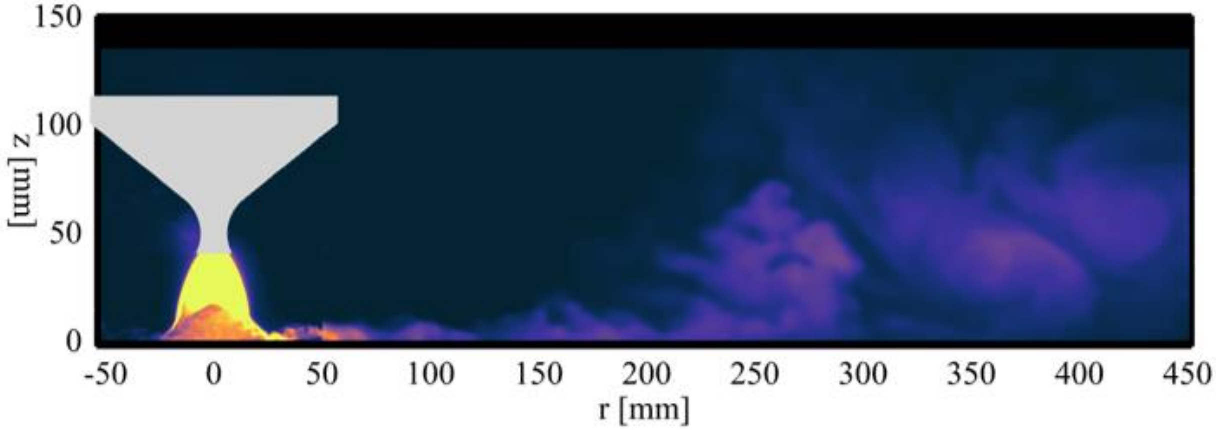

(a) $t = \tau$

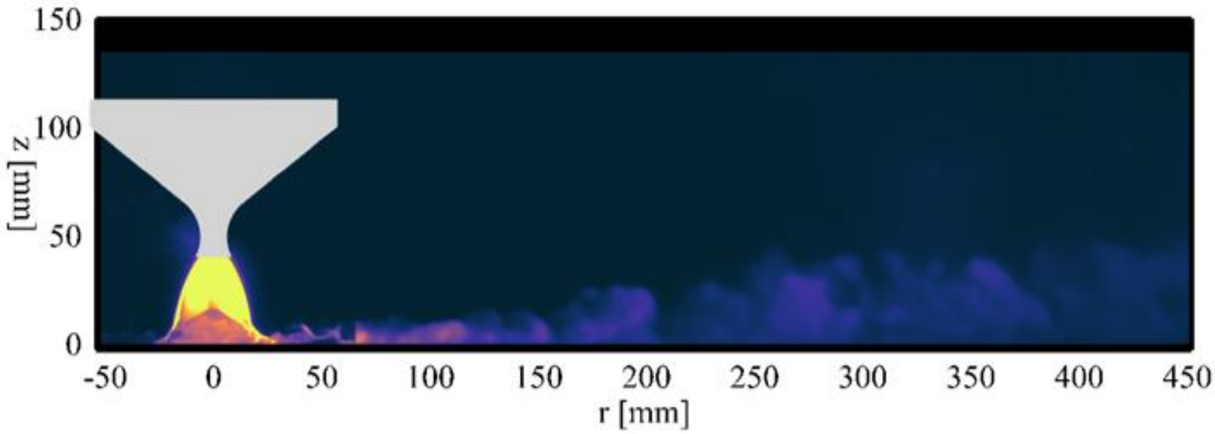

(b) $t = \tau + 0.1$ s

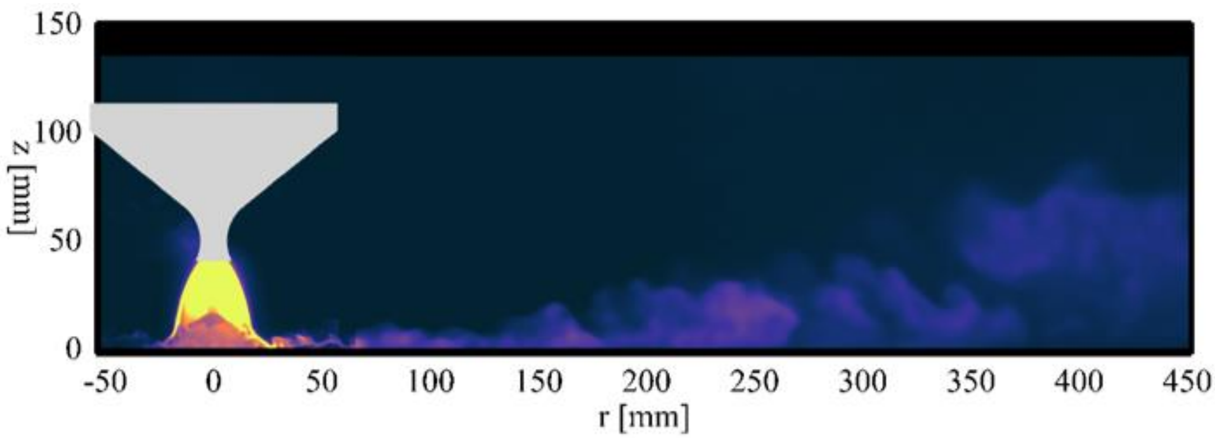

(c) $t = \tau + 0.2$ s

Fig. 7. Combined simultaneous instantaneous PLIF image from the two camera views, shown in a linear intensity scale, illustrating the plume impingement and wall-jet evolution (right) during jet start-up at $h/D_e = 3$ and $P_a = 584$ kPa (Case III): (a) $P_0 = 743$ kPa, (b) $P_0 = 830$ kPa, and (c) $P_0 = 794$ kPa. The image in (a) is estimated to be $\tau = 0.02$ s from opening of the nozzle solenoid valve.

increased radial distances can be clearly seen. Most curiously, significant large flow structures extending in the vertical direction beyond z = 100 mm near r = 250 mm are apparent in the image shown in Fig. 7(a), which was acquired within 100 ms of jet impingement. The subsequent images at 0.1 s intervals show vertical structures reaching approximately z = 50 mm in Fig. 7(b) and up to approximately z = 75 mm in Fig. 7(c). The initial impact of the plume with the surface is still a largely unexplored area in the literature and it is possible that the physics of initial plume impingement creates an especially large wall-jet while the steady-state wall jet is smaller. Further investigation of this behavior would help clarify and mitigate risks posed by ejecta transport in the wall-jet to the nearby infrastructure of a landing site, especially from landers operating in a pulsed plume configuration. While the chosen color scale in Fig. 7 saturates the higher density region of the primary plume upstream of the stagnation shock, it reveals some aspects of the region immediately below the stagnation shock. The complex fluid dynamics and kinematics in this region, especially in terms of velocity gradients, are also largely unexplored but are believed to have significant influence on the potential cratering at a landing site.

IV. Summary and Ongoing Work

PLIF imaging performed on a supersonic jet impinging on a flat plate in a vacuum environment is described in this work. Images showing the spatial evolution of the wall-jet are presented for select test conditions, where a secondary PLIF camera was available to capture the wall-jet evolution simultaneously with the primary PLIF camera, which captured the primary plume impingement. The canonical configuration experimentally studied in this work is representative of the plume-surface interaction induced by a rocket exhaust plume impinging on the planetary surface in lunar and Martian environments. The behavior of the wall-jet, in particular, has implications for ejecta transport, which has the potential for damaging nearby infrastructure on the Moon or Mars. Three unique test conditions are presented in this paper: two at lunar-relevant conditions and one at Martian-relevant conditions. Both lunar-relevant conditions exhibited laminar behavior. However, very different flow features are seen for the plume impingement region and also for the lifted nature of the wall-jet between these two conditions. In addition to showing a third distinct plume-impingement behavior, the Martian-relevant case revealed a highly unsteady wall-jet. The unsteadiness, hypothesized to be due to a physical process similar to a Kelvin–Helmholtz instability, results in the dramatic expansion of the wall-jet height with increased radial distances. Further efforts are needed to characterize the wall-jet evolution, especially in terms of the multiphase ejecta transport, to help clarify and mitigate risks posed by ejecta transport in the wall-jet to the nearby infrastructure of a landing site. In particular, investigation of the transient start-up behavior of the wall-jet and transients of a pulsed plume configuration could be investigated using emerging high-speed PLIF visualization and velocimetry techniques [16].

Acknowledgments

The ground test reported in this work was supported by the NASA Space Technology Mission Directorate (STMD) Game Changing Development (GCD) program *Plume Surface Interaction* with S. Harris from NASA Marshall Space Flight Center (MSFC) serving as project manager. The authors thank Dr. Ashley M. Korzun and Dr. Manish Mehta for setting the initial direction of this work. The authors also acknowledge the technical input from Dr. Jeff West, Dr. Andrew Weaver, and Thomas Shurtz from MSFC. The measurements reported in this paper were part of a larger ground test campaign and several people from MSFC are acknowledged for these efforts, including Dr. Chad Eberhart, Kristopher McDougal, Tracy Reynolds, Tom Liu, Jeffrey Rayburn, Howard Soohoo, Kevin Thompson, Dr. Jim Sisco, Kristian Miasek, and Kevin Baker. Finally, the authors also thank W. Holt Ripley from the NASA Langley Research Center for assistance with preparation and shipment of PLIF equipment to the test facility, Dr. Timothy Fahringer for assistance with the view A image dewarping, and J. Sebastian Rubio from the Johns Hopkins University for assistance with the PLIF setup in the vacuum chamber.

References

[1] Korzun, A. M., Eberhart, C. J., West, J., Liever, P., Weaver, A., Mantovani, J., Langton, A., Kemmerer, B., and Atkins, A. "Design of a Subscale, Inert Gas Test for Plume-Surface Interactions in a Reduced Pressure Environment," AIAA 2022-1808. *AIAA SCITECH 2022 Forum*. January 2022.

[2] Eberhart, C. J., West, J., and Korzun, A. M. "Overview of Plume-Surface Interaction Data from Subscale Inert Gas Testing at NASA MSFC Test Stand 300 Vacuum Facilities," AIAA 2022-1810. *AIAA SCITECH 2022 Forum*. January 2022.

[3] Diaz-Lopez, M. X., Gorman, M., Rubio, J. S., and Ni, R. "Plume-surface Interaction Physics Focused Ground Test 1: Diagnostics and Preliminary Results," AIAA 2022-1809. *AIAA SCITECH 2022 Forum*. January 2022.

[4] Rubio, J. S., Gorman, M., Diaz-Lopez, M. X., and Ni, R. "Plume-Surface Interaction Physics Focused Ground Test 1: Setup and Preliminary Results," AIAA 2022-1809. *AIAA SCITECH 2022 Forum*. January 2022.

[5] Gorman, M. T., Rubio, J. S., Diaz-Lopez, M. X., Chambers, W. A., Korzun, A. M., Rabinovitch, J., and Ni, R., "Scaling laws of plume-induced granular cratering," PNAS nexus 2(9), 2023. doi: 10.1093/pnasnexus/pgad300.

[6] Danehy, P. M., Weisberger, J., Johansen C., Reese, D., Fahringer, T., Parziale, N. J., Dedic C., Estevadeordal, J., and Cruden, B. A., "Non-Intrusive Measurement Techniques for Flow Characterization of Hypersonic Wind Tunnels," *NATO STO Manuscript on Hypersonic Freestream Characterization*, 2018.

[7] Rodrigues, N. S., Tyrrell, O. K., Danehy, P. M., Eberhart, C. J., McDougal, K. J., Liu, T., Reynolds, T. D., Rubio, J. S., Jiang, N., Hsu, P., and Korzun, A. M. "Flow Visualization for Plume-Surface Interaction Testing Within Large-Scale Vacuum Environments at Conditions Relevant to Lunar and Martian Landers", *JANNAF Exhaust Plume and Signatures Annual Meeting*. December 2023.

[8] Rodrigues, N. S., Tyrrell, O. K., and Danehy, P. M., "Fluorescence imaging of plume-surface interaction in large-scale reduced pressure environments," *Physics of Fluids* 36:10, 2024. doi: 10.1063/5.0223210.

[9] Tyrrell, O. K., Rodrigues, N. S., Korzun, A. M., and Danehy, P. M. "Flow visualization of intrusive and non-intrusive configurations for lunar- and Martian-relevant plume-surface interaction," AIAA 2024-2499. *AIAA SCITECH 2024 Forum*. January 2024. doi: 10.2514/6.2024-2499.

[10] Rodrigues, N. S., Tyrrell, O. K., Eberhart, C. J., McDougal, K. J., Korzun, A. M., and Danehy, P. M. "Flow Visualization for Plume-Surface Interaction at Martian-relevant Lander Environments," AIAA 2024-4914. *AIAA ASCEND 2024 Forum*. July 2024. doi: 10.2514/6.2024-4914

[11] Rubio, J. S., Diaz-Lopez, M. X., Gorman, M., Ni, R., and Rodrigues, N. S., "On the Interaction Between a Flow Instability and Inertial Particles in Supersonic Jet Plume-Surface Interaction," AIAA 2025-XXX. *AIAA SCITECH 2025 Forum*. January 2025.

[12] Cuesta, C. J., Davies, J., Worrall, K., Cammarano, A., and Zare-Behtash, H., "Plume-surface interactions: A review paper of experimental work," *Acta Astronautica* 226(1), 2025. doi: 10.1016/j.actaastro.2024.09.021.

[13] Rodrigues, N. S., Bathel, B., Danehy, P. M. "A Comparison of NO Laser-induced Fluorescence Models at conditions relevant to Supersonic and Hypersonic Flows", AIAA 2022-0897. *AIAA SCITECH 2022 Forum*. January 2022.

[14] Tsai, R., "A versatile camera calibration technique for high-accuracy 3D machine vision metrology using off-the-shelf TV cameras and lenses," *IEEE Journal on Robotics and Automation* 3(4), 1987. doi: 10.1109/JRA.1987.1087109.

[15] Schwartz, R. J. "ViDI: the Virtual Diagnostics Interface", NASA CR-2004-212667. October 2004.

[16] Rodrigues, N. S., Jiang, N., Hsu, P., Roy, S., and Danehy, P. M., "Multiline molecular tagging velocimetry of nitric oxide at 100 kHz using an injection-seeded burst-mode OPO," *Applied Optics* 63(5), 2024. doi: 10.1364/AO.507732.